

# Active Plasmonic Colloid-to-Film-Coupled Cavities for Tailored Light–Matter Interactions

Fabian R. Goßler,<sup>†,‡</sup> Anja Maria Steiner,<sup>†,‡</sup> Oleksandr Stroyuk,<sup>§,||</sup> Alexandra Raevskaya,<sup>§,||</sup> and Tobias A. F. König<sup>\*,†,‡</sup>

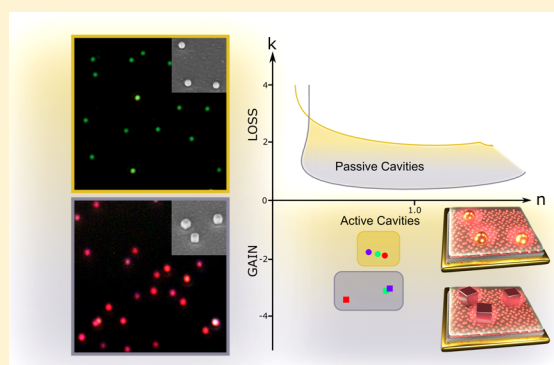
<sup>†</sup>Leibniz-Institut für Polymerforschung Dresden e.V., Institute for Physical Chemistry and Polymer Physics, Hohe Str. 6, 01069 Dresden, Germany

<sup>‡</sup>Cluster of Excellence Centre for Advancing Electronics Dresden and <sup>§</sup>Physical Chemistry, TU Dresden, 01069 Dresden, Germany

<sup>||</sup>L.V. Pysarzhevsky Institute of Physical Chemistry, National Academy of Sciences of Ukraine, 01030 Kiev, Ukraine

## Supporting Information

**ABSTRACT:** For large-scale fabrication of optical circuits, tailored subwavelength structures are required to modulate the refractive index. Here, we introduce a colloid-to-film-coupled nanocavity whose refractive index can be tailored by various materials, shapes, and cavity volumes. With this colloidal nanocavity setup, the refractive index can be adjusted over a wide visible wavelength range. For many nanophotonic applications, specific values for the extinction coefficient are crucial to achieve optical loss and gain. We employed bottom-up self-assembly techniques to sandwich optically active ternary metal-chalcogenides between a metallic mirror and plasmonic colloids. The spectral overlap between the cavity resonance and the broadband emitter makes it possible to study the tunable radiative properties statistically. For flat cavity geometries of silver nanocubes with sub-10 nm metallic gap, we found a fluorescence enhancement factor beyond 1000 for 100 cavities and a 112 meV Rabi splitting. In addition, we used gold spheres to extend the refractive index range. By this easily scalable colloidal nanocavity setup, gain and loss building blocks are now available, thereby leading to new generation of optical devices.



## INTRODUCTION

Plasmonic cavity-coupled emitters are highly appealing systems to study light–matter interactions due to their strong and confined nearfield enhancement upon excitation.<sup>1</sup> Such systems have proven to be promising candidates for tailoring photonic properties at exceptionally small mode volumes.<sup>2,3</sup> Recently, colloidal approaches have been introduced to continue this development by incorporating the emitting material (molecular excitons or quantum dots (QDs)) using host–guest chemistry,<sup>4</sup> simple immersion techniques,<sup>5</sup> or polyelectrolyte multilayers.<sup>6</sup> The fast energy transfer between excitonic quantum emitters and the cavity system leads to hybridized light–matter states provided that the plasmon–exciton coupling is sufficient.<sup>7,8</sup> To exploit these sub-wavelength-scale phenomena for applications like optical circuits and calculations, the refractive index (RI) ( $\tilde{n} = n + ik$ ) of the structure itself must be modulated.<sup>9</sup> Most computational metastructures are based on alternating the real part of the refractive index through implementation of different dielectric materials. In these periodic arrangements, the materials are chosen such that the index contrast in the real part  $n$  is maximized, whereas the imaginary part  $k$  is minimized to reduce losses.<sup>10</sup> These conditions are often met using ordered polymer structures.<sup>11</sup> However, a high refractive index contrast with a spatial variation below the diffraction limit is desirable for

application in transformation optics,<sup>12</sup> such as cloaking,<sup>13</sup> field concentration,<sup>14</sup> and perfect absorbers.<sup>15</sup> To achieve this, plasmonic nanostructures can be used instead of dielectric materials. The material refractive index contrast can be increased significantly if a noble metal ( $n < 1$  due to free electrons) is used instead of a dielectric material ( $n \sim 1.4$ ). When noble metals are used, greater absorptive losses are generally encountered, but these losses are not overly problematic because the plasmonic structures feature much higher coupling interactions than dielectric structures.<sup>16</sup> In other words, the imaginary index can be also used as a material contrast property. This is shown in the recent developments in the field of passive parity-time metamaterials, where contrasts in both  $n$  and  $k$  are utilized to provide a unidirectional light propagation.<sup>17</sup> If optically active materials like molecular excitons or quantum dots are now coupled to such structures,  $k$  can be further modulated to become negative (single-mode lasing).<sup>18</sup> These active parity-time metamaterials might be an important step toward next-generation optical applications on a subwavelength scale.<sup>18</sup>

Received: December 31, 2018

Revised: February 15, 2019

Published: February 19, 2019

Here, we study the radiative properties for a set of colloid-to-film-coupled cavities as determined by their composition. We combine a well-defined self-assembled monolayer (SAM) of thiolates with a polymeric film formed using layer-by-layer deposition methods to achieve a homogeneous and emitting spacer layer of various thicknesses. Gold spheres and silver cubes are used as plasmonic colloids, and ternary metal-chalcogenide quantum dots with a long photoluminescence (PL) lifetime (100 ns) and broad emission range (full width at half-maximum (FWHM) = 304 meV) are chosen as the optically active material. By using a combination of surface and optical characterization methods, we can establish the presence of light–matter interactions and study the optical properties statistically. An improvement in electromagnetic simulation methods allows us to calculate the effective refractive index for each system. This quantification combined with self-assembly makes the colloid-to-film-coupled cavities potentially useful for the next generation of optical circuits.

## EXPERIMENTAL METHODS

**Substrate Preparation.** A gold film with a thickness of 50 nm was evaporated onto a clean glass slide (Menzel) using physical vapor deposition (HEX-L by Korvus Technology Ltd, Newington, U.K.). The gold layer thickness was validated using spectroscopic ellipsometry (J.A. Woollam, RC2 Ellipsometer) to be 50 nm. The substrate was then incubated in a 1 mM solution of (11-mercaptoundecyl)-*N,N,N*-trimethylammonium bromide (MUTAB) (Sigma Aldrich) to form a positively charged self-assembled monolayer. The thickness was determined to be 1.5 nm using spectroscopic ellipsometry. A monolayer of thioglycolic acid (TGA) functionalized silver–indium–sulfide (AgInS) quantum dots was assembled by placing the sample into an aqueous QD dispersion for 30 min at room temperature. The formation of a homogeneous layer of AgInS QDs was verified using fluorescence lifetime imaging (FLIM) and atomic force microscopy (AFM). An additional polymeric spacer was applied by (repeatedly) dip-coating the sample into (alternating) solutions of poly(allylamine hydrochloride) (PAH) (0.1 mg/mL; 0.5 mM NaCl) and poly(styrene sulfonate) (PSS) (0.1 mg/mL; 0.5 mM NaCl) each for 60 s. Between each layer-by-layer assembly step, the sample was rinsed with ultrapure water (Merck Millipore) for 30 s. Each PAH/PSS monolayer is estimated to be 1–2 nm in thickness, as measured by ellipsometry. The metallic nanoparticles were applied by drop-casting onto the substrate for 30 s, followed by rinsing with purified water and nitrogen drying.

**Dark-Field Measurements.** Single-particle scattering spectroscopy was done with a Nikon Ti-U inverted microscope in transmission mode. The data were recorded using an IsoPlane-160 spectrometer and a PIXIS: 256 charge-coupled device camera (Princeton Instruments). Measurements were performed with a dark-field condenser (air, NA 0.8–0.95) and a 60× air objective (CFI S Plan Fluor ELWD, NA 0.7, Nikon, Japan) under illumination by an Energetiq EQ-99 laser-driven light source. The measured spectra were corrected by subtracting the dark current at the detector and normalizing against the white light scattering spectrum of a polystyrene particle solution.

**Time-Resolved Fluorescence Measurements.** Fluorescence lifetime images and time-correlated single-photon counting (TCSPC) data were measured with an inverted confocal scanning microscope (MT200, PicoQuant) incorporating a 100× air objective (UPLFLN, NA 0.9, Olympus, Japan).

Diode lasers with 405 and 506 nm central wavelengths (LDH-405; LDH-510) and 1–5 MHz repetition rates were used for excitation. The signal was guided through a long pass filter with a cutoff below 519 nm (FF01-519/LP, Semrock) and detected with a SPCM-AQRH single-photon counting module (Excelitas).

**Photoluminescence (PL) Measurements.** The spectrum of the AgInS QD monolayer was detected with an Andor SR 163 Spectrograph during continuous exposure with a 405 nm diode laser (LDH-405). The background correction was done by dark current measurement.

**Synthesis of Plasmonic Nanoparticles.** Hexadecyltrimethylammonium chloride (CTAC) capped gold nanospheres were synthesized by a seed-mediated growth process, as described by Steiner et al.<sup>19</sup>

Briefly, the particles were synthesized in three steps. First, tetrachloroauric acid ( $\text{HAuCl}_4$ ) was reduced by sodium borohydride ( $\text{NaBH}_4$ ) in the presence of hexadecyltrimethylammonium bromide. The obtained 2 nm single-crystalline seeds were successively grown up within the next two steps to receive spherical particles of about 70 nm. For the growing process,  $\text{HAuCl}_4$ , CTAC, and ascorbic acid serve as Au precursor, stabilizing agent, and reductant, respectively. To ensure kinetic control, a syringe pump was used in the last step.

CTAC-capped silver nanocubes were synthesized by a living silver overgrowth of gold nanospheres, as recently published by Mayer et al.<sup>20</sup>

**Synthesis of Quantum Dots.** AIS/ZnS core/shell QDs were prepared in aqueous alkaline solutions as described in detail in recent literature.<sup>21,22</sup> Briefly, core AIS QDs were formed via the interaction between sodium sulfide and a mixture of Ag(I) and In(III) complexes with thioglycolic acid (TGA). The reaction was performed in deionized (DI) water at 96–98 °C in the presence of ammonia and was complete in 60 min. A ZnS shell was subsequently formed over the AIS cores by the addition of a Zn(II)–TGA complex. In this step, the colloidal solution remained at 96–98 °C for additional 10 min. The AIS/ZnS QDs were then precipitated by introducing an excessive amount of 2-propanol separating the precipitate from the supernatant by centrifugation and redispersing in pure DI water. The procedure yields stable colloidal AIS/ZnS solutions with a molar Ag(I) concentration of up to 0.1 M. The atomic ratio of metals in the final AIS/ZnS QDs was kept at Ag/In/Zn = 1:4:8.

**Finite-Difference Time-Domain (FDTD) Simulations.** A commercial-grade simulator based on the finite-difference time-domain (FDTD) method was used to perform the calculations (Lumerical FDTD, version 8.16).<sup>23</sup> To simulate the optical response, a total-field scattered-field source was used, and the frequency points were set to be half the wavelength span. We used perfectly matched the layer boundary conditions (BC) in all principal directions with a linearly polarized plane wave source ( $\lambda = 300\text{--}800$  nm). Monitor boxes were used to obtain the optical responses of the system. For the dielectric properties of gold and silver, data from Johnson and Christy<sup>24</sup> and CRC<sup>25</sup> were fitted using six coefficients for gold and five for silver. Both fits had a root-mean-square (RMS) error of 0.2. For simulating the coupling interactions, we added a Lorentz Oscillator to resemble the optically active layer inside the cavity. All simulations reached an auto-shut-off of at least  $10^{-5}$  before reaching 300 fs simulation time. For the best simulation stability, the mesh area was chosen to be at least 100 nm larger than the existing structure in all three principal directions. For the simulation of the coupling interactions, we employed a Lorentz

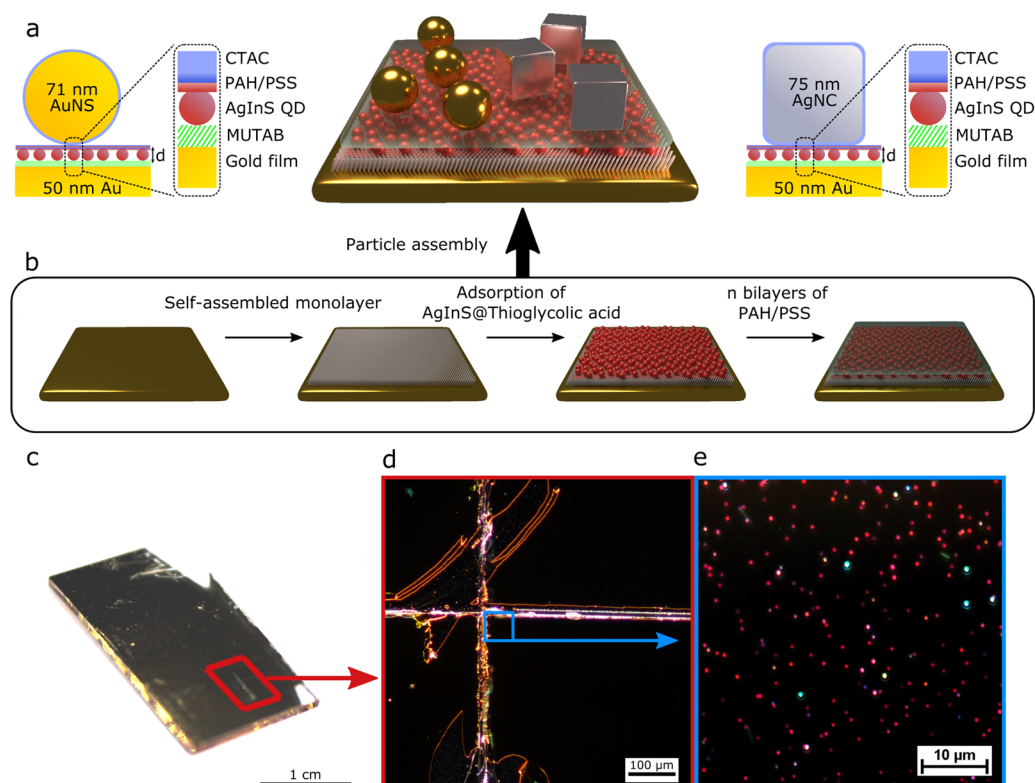


**Figure 1.** Setup of the macroscopic colloid-to-film-coupled nanosystem: (a) schematic description of the colloid-to-film nanocavity for a gold nanosphere (left) and a silver nanocube (right) coupled to a gold film with ternary metal-chalcogenide quantum dots sandwiched between colloid and film. (b) Fabrication steps required to form the uniform emitting spacer layer. (c) A photograph of an as-prepared substrate containing self-assembled cavities. (d) Dark-field microscopy image of the sample in (c) with two engraved orientation lines. (e) Dark-field microscopy image of the area marked in (d) showing colloid-to-film-coupled nanocavities.

model layer inside the cavity spacing. For effective refractive index calculations, the FDTD  $S$ -parameter extraction analysis was used.<sup>26</sup> To retrieve the optical constants for the inhomogeneous asymmetric structure, we calculated the optical response in the forward ( $S_{12}/S_{22}$ ) and reverse ( $S_{11}/S_{21}$ ) directions. For these simulations, the automatic shut-off level was adjusted to  $10^{-7}$ . For all simulations with and without dipoles (to simulate a dipole-free situation, the dipole amplitude was set to 1/10), we ensured that the electromagnetic fields propagated as a plane wave (uniform fields) by introducing an electric field monitor at a sufficient distance from the structure ( $1\ \mu\text{m}$ ). We used periodic BCs in plane, a perfectly matched layer BC in the beam direction and a linearly polarized plane wave source ( $\lambda = 300\text{--}800\ \text{nm}$ ). The simulation setup was placed in the center of the FDTD simulation surrounded by air ( $n = 1$ ). Metamaterial span as well as metamaterial center was set to the colloid-to-film-coupled setup accordingly.

## RESULTS AND DISCUSSION

The fabrication of our colloidal nanocavities starts with a self-assembled monolayer of (11-mercaptoundecyl)- $N,N,N$ -trimethylammonium bromide that is adsorbed on a gold film as a 1.5 nm layer (see Figure 1). This method proved to be suitable for the bottom-up self-assembly, since thiolate-based self-assembled monolayers SAMs on gold are easy to generate and offer ordered monolayers on a macroscopic scale.<sup>27–29</sup> Therefore, the surface charge is uniformly distributed and allows the negatively charged silver–indium–sulfide (AgInS) particles (3 nm) to be adsorbed in a homogeneous monolayer. We get a homogeneously distributed monolayer of emitters with an estimated quantum

dot density of  $6.5 \times 10^{12}$  emitters per  $\text{cm}^2$  (Figure S1). To tune the distance between the metallic surfaces and ensure a homogeneous surface, additional polymer spacing was applied using the well-known layer-by-layer assembly method involving PAH and PSS.<sup>30,31</sup> Thus, the distance between the metal surfaces was adjusted by including different amounts of polyelectrolyte bilayers. Uniform coverage and low surface roughness of the spacing-emitter layer was verified via atomic force microscopy (AFM, Figure S2), scanning electron microscopy (SEM, Figure S3), and FLIM measurements (Figure S4). By AFM, an RMS surface roughness of 2.045 nm was measured on a  $15 \times 15\ \mu\text{m}^2$  area, and a uniform fluorescence emission signal was detected. The plasmonic colloids were then applied using drop-casting. For the CTAC surfactant layer surrounding the nanoparticles, we estimated a thickness of 2 nm from simulations. The final cavity spacing  $d$  is therefore made up of the thiolate SAM (1.5 nm), AgInS QDs (3 nm), a variable PAH/PSS multilayer, and a surfactant around the particles (2 nm). To ensure that the cavities were built from single particles, further SEM measurements and dark-field microscopy were employed to study the prepared substrates (Figures S5 and S6). This combination of self-assembled monolayers and colloidal building blocks makes it possible to manufacture a variety of stable cavity systems featuring different spacings and geometries with low fabrication efforts. A complementary and statistical study on their radiative properties is now possible.

Figure 2 shows a general evaluation of the different cavity designs chosen to cover a broad range of cavity resonances and light–matter interactions. For quantitative information about the single cavities and their exciton-coupling, single-particle

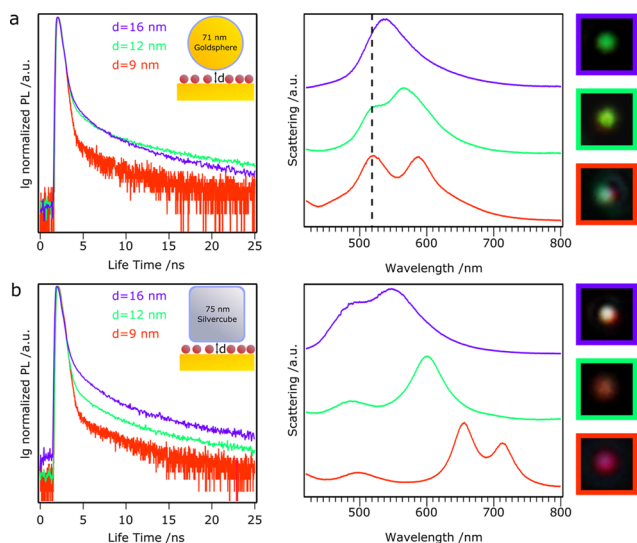


**Figure 2.** Spectroscopic properties of various colloid-to-film-coupled setups: time-correlated single-photon counting, scattering spectroscopy, and dark-field imaging of (a) gold spheres and (b) silver cubes coupled to a gold film with 9 nm (red), 12 nm (green), and 16 nm (purple) cavity spacing. The dashed line in (a) marks the gold film scattering.

scattering spectroscopy and TCSPC were used to directly access the optical properties of the colloid-to-film-coupled cavities. The TCSPC decay rate measurements of gold spheres and silver cubes were highly sensitive to the particle-to-film distance  $d$ . For gold spheres with 12 and 16 nm spacings, similar TCSPC curves

were obtained, whereas the 9 nm cavity led to a significantly enhanced decay rate. Silver cubes offer a greater degree of decay rate changes as a clear trend toward shorter lifetimes was detected for decreasing particle-to-film distances. This effect becomes more comprehensive when the single cavity scattering spectra are taken into account. Both particle systems show coupling interactions with the gold mirror as expressed through a spectral redshift. The silver cubes show a large sensitivity  $\frac{\Delta\lambda}{\Delta d}$  of 23.7, whereas the gold spheres were less sensitive at 7.1. The higher sensitivity of the cube setup is dominated by the edge geometry rather than the material properties of silver (Figure S7). This relationship is also observable through dark-field microscopy as shown in Figure 2. Whereas only minor changes of the color of the cavity scattering cross section are visible for the sphere-to-film geometry, a more pronounced color variation takes place for the cube-to-film systems. The pronounced peak at 520 nm in the sphere-to-gold film system is caused by scattering of the gold film and not visible in the cube-to-gold film geometry due to the much higher scattering intensity of the silver cubes compared to gold spheres. The most significant observation is the Rabi splitting of the cavity resonance for the sub-10 nm cube-to-gold film gap. This mode hybridization is a signature that light–matter interactions between the plasmonic and the excitonic systems are becoming strong enough to overcome the energetic losses of the resonator. Since light–matter interactions are necessary for optical gain, we further investigated the optical properties of this particular 9 nm silver cube cavity setup.

To evaluate the suitability of the cube-to-gold-film-coupled cavities for tasks that demand strong plasmon–exciton

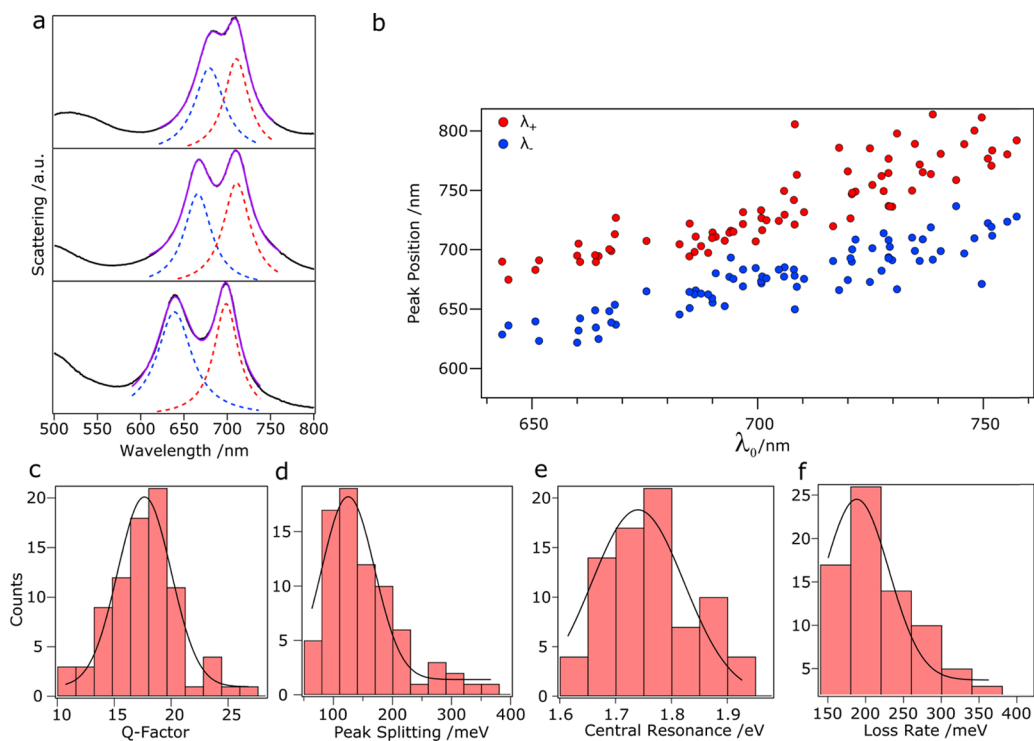


**Figure 3.** Statistical evaluation of silver cube nanocavities at 9 nm spacing: (a) dark-field scattering spectra of three representative nanocavities. The solid black line shows the measured scattering response. The blue and red dashed lines show the individual Lorentzian fits and the purple solid lines show the combined fits. (b) Peak position of the hybridized modes with respect to the estimated cavity resonance  $\lambda_0$ . (c–f) Histogram plots and Gaussian fits (black lines) of (c) Q-factor, (d) peak splitting, (e) cavity resonance, and (f) loss rate. Seventy-seven nanocavities were studied statistically.

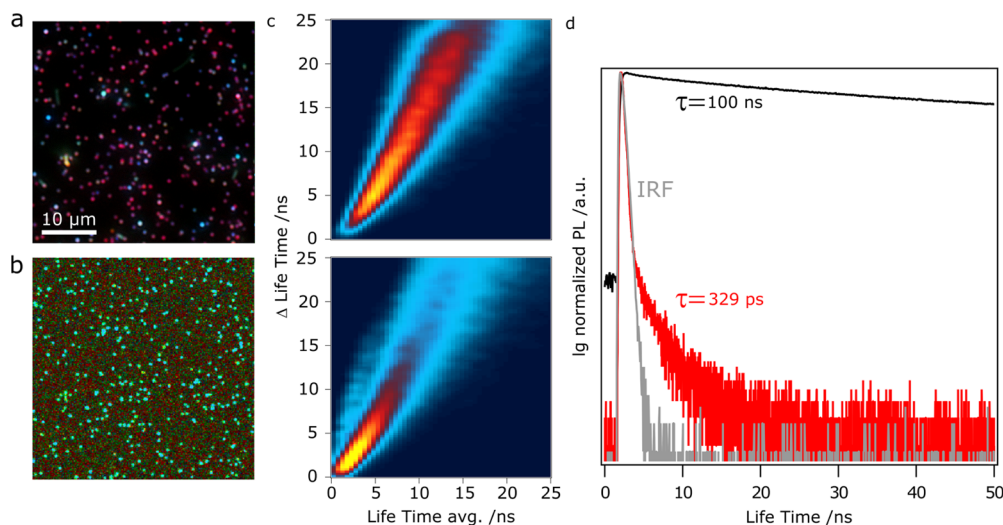


**Figure 4.** Dark-field spectroscopy and time-correlated single-photon counting in cube-to-film-coupled cavities: (a) dark-field scattering image of silver cube nanocavities at 9 nm spacing. (b) Fluorescence events (gray scale) and fluorescence lifetime (color scale) image of the corresponding cavities in (a). (c) Lifetime pattern images of quantum dot monolayers without (top) and with (bottom) silver cubes. (d) Normalized photoluminescence (PL) measurements of the ensemble of quantum dots on glass (black) and a single cavity (red). The instrument response function is shown in gray.

interactions, we need to quantify the occurring losses  $\gamma$  as well as the coupling strength  $g$ . Another point of interest is the quality factor  $Q$ , which is a measure of the energetic losses with respect to the resonance wavelength of an optical resonator. Our colloidal approach enables statistical measurements of the optical properties of single cavities by dark-field scattering spectroscopy. The required parameters can directly be extracted from the resulting spectra, since  $\gamma$  is the spectral FWHM, whereas  $g$  is given by the distance between the hybridized plasmon peaks.<sup>32</sup> This can be understood by applying a coupled-oscillator model

$$\omega_{\pm} = \frac{1}{2}(\omega_{\text{cav}} + \omega_0) \pm \sqrt{g^2 + \frac{\delta^2}{4}} \quad (1)$$

where  $\omega_{\pm}$  is the frequency of the hybrid modes,  $\omega_{\text{cav}}$  is the cavity frequency,  $\omega_0$  is the emitter frequency,  $g$  is the coupling strength, and  $\delta$  is the detuning between cavity and emitter resonance. As Figure 3 shows, we evaluated 77 cube-to-film-coupled cavities and extracted the desired parameters using Lorentzian functions (Figure 3a). To visualize the optical range in which our cavities are operational, we also obtained the estimated cavity wavelength  $\lambda_0$  for each spectrum (Figure 3b) by using an additional Lorentzian fit. We found the mean quality factor of the 9 nm cube system to be  $16.9 \pm 0.2$ , whereas typical plasmonic cavities have  $Q$ -factors between 5 and 10, although similarly high  $Q$ -factors were reported for different cavity geometries.<sup>16,32</sup> The statistical analysis of coupling strength gives a normal distribution with a mean value of  $111.5 \pm 5.2$  meV, which is of the same order of magnitude as published in literature recently.<sup>7</sup> The variations of the coupling strengths are affected by several parameters. On the one hand, the absolute position of the emitters is crucial. Cube-to-metallic-film-coupled cavities induce large field enhancements near the edges of the cubes and lower field strengths in the center. Varying positions of the AgInS particles in each cavity will therefore lead to different levels of interaction. On the other hand, the number of emitters  $N$  also affects the cavity coupling.<sup>33,34</sup> For the cube-to-film geometry, we have an estimated  $N$  of 360 emitters per cavity (Figure S1). The estimated average central wavelength of the

coupling cavities is found to be 720 nm ( $1.72 \pm 0.01$  eV), which matches the emission from the AgInS QD monolayer (Figure S8). The mean losses of the cavities are found to be  $177.5 \pm 6.5$  meV. Although the loss surpasses the coupling strength in general, we can still observe plasmonic mode hybridization, which is usually associated with strong plasmon–exciton coupling. Latter is defined by  $2g > \gamma$ , which is only the case for several of the detected cavities (Figure S9). The statistical evaluation shows that the cavities feature stable conditions concerning their light–matter interactions. Together with the scalable manufacturing process, they can be employed in macroscopic applications in the future.

One of the most promising ways to employ plasmonic cavities is their impact on the emitters' decay channels. Due to the QDs' close proximity to the metal surfaces, the excitable states of the quantum dots are altered, leading to both faster radiative and nonradiative decays.<sup>35</sup> Since the increase in radiative decay rates generally exceeds that of the nonradiative channels, the overall quantum efficiency of the QD emission improves significantly. This gives rise to photoluminescence enhancement, which results in a strong increase in emission. Figure 4a shows a dark-field microscopy image of the cube-to-gold-film-coupled cavities sandwiching the AgInS QD monolayer, verifying the presence of a cube-to-gold-film-coupled nanocavities. Figure 4b shows the same area as a FLIM, in which the contrast resembles the photoluminescence intensity and the color indicates the lifetime. A strong increase in the emission intensity can be detected at each cavity. To quantitatively analyze the photoluminescence enhancement, we determined the enhancement factor (EF), which is defined as

$$\text{EF} = \frac{I_{\text{cav}} A_{\text{fit}}}{I_{\text{bkg}} A_{\text{cav}}} \quad (2)$$

$I_{\text{cav}}$  is the emission intensity of the cavity,  $I_{\text{bkg}}$  is the intensity of the AgInS QD monolayer outside the cavity,  $A_{\text{fit}}$  is the area of the enhanced region, and  $A_{\text{cav}}$  is the estimated area of the cavity. The data were extracted from each cavity by applying a two-dimensional Gaussian fit, in which  $I_{\text{cav}}$  describes the amplitude,  $I_{\text{bkg}}$  the baseline, and  $A_{\text{fit}}$  the FWHM of the fit.  $A_{\text{cav}}$  was assumed

to be  $75 \times 75 \text{ nm}^2$ . A statistical evaluation of 100 cavities gives an EF of  $1002 \pm 48$  for the cube-to-gold-film-coupled nanocavities.

For application in devices like optical circuits, it is necessary to modulate the decay rates of the emitters in a controlled fashion. Since the lifetime is inversely proportional to the decay rate, a decrease is to be expected for plasmonically enhanced fluorescence. TCSPC was employed to further quantify the radiative decay properties of the cavities. Whereas uncoupled AgInS emitters show an estimated average lifetime of 100 ns, the metal-enhanced photoluminescent system shows a drastically decreased lifetime of about 330 ps (Figure 4d), which is nearly indistinguishable from the instrument response function for most of the measured photons. Both the improved emission and the enhanced exciton decay indicate a strong interaction between plasmonic and excitonic components of the system. To study the macroscopic changes in emission behavior for cube-to-gold-film-coupled cavities, we employed a lifetime pattern analysis of FLIM measurements that provides information about the general lifetime distributions of a measured surface. Figure 4c shows the lifetime pattern of an AgInS QD monolayer on gold without (top) and with (bottom) plasmonic colloids. Although only about 2.5% of the surface is affected by the plasmonic cavities, we observed strong confinement of the lifetime distribution at high decay rates. This shows that our colloidal approach is suitable for the large-scale modulation of the radiative properties in enhancement and lifetime.

Since complementary experimental findings have pointed toward the presence of significant plasmon–exciton coupling in our cavity systems, their actual suitability as optical loss and gain materials was studied using FDTD simulations. The correspondence between refractive index and spatial location is crucial for applications such as transformation optics or nonreciprocal light propagations. We used the S-parameter method to determine the refractive index of our colloid-to-film-coupled cavity, which was calculated for an area of  $300 \times 300 \text{ nm}^2$  (see Figure 5). For this, the colloidal cavity was excited in both forward and backward directions, from which a transfer matrix with four elements was determined (S-matrix). Together with the size and position of the cavity, the effective refractive index was calculated. The first step in FDTD S-parameter calculations is the comparison of the results with values from literature (see also Figure S10). The comparison of the bulk refractive index values for gold<sup>24</sup> and silver<sup>25</sup> also indicates the total range in which the index of the gold/silver colloidal cavity can be modulated. Starting with a gold sphere as colloid, the imaginary refractive index/extinction coefficient ( $k$ ) could be changed significantly (60%) with respect to the literature values for gold, whereas the real refractive index ( $n$ ) changes only slightly (10%). These complex index values correspond to earlier published data that were used to quantify a colloidal magnetic metasurface.<sup>36,37</sup> Loops are observed in the index modulation diagrams for silver cubes, and these loops vary as the cavity spacing is adjusted. This effect is attributed to the flat cavity geometry, which causes a clear and strong cavity resonance between 600 and 750 nm. The loops in the index diagram of Figure 6 are to be interpreted as resonances (Lorentz oscillation). These resonances result in a peak in the real part of the refractive index, whereas the imaginary part is similar to a derivative of the peak. Figure S9 shows the real and imaginary parts of the refractive index with respect to wavelength. Given the resonance form, the same real refractive index can occur at different wavelengths. The same applies to the imaginary part. It

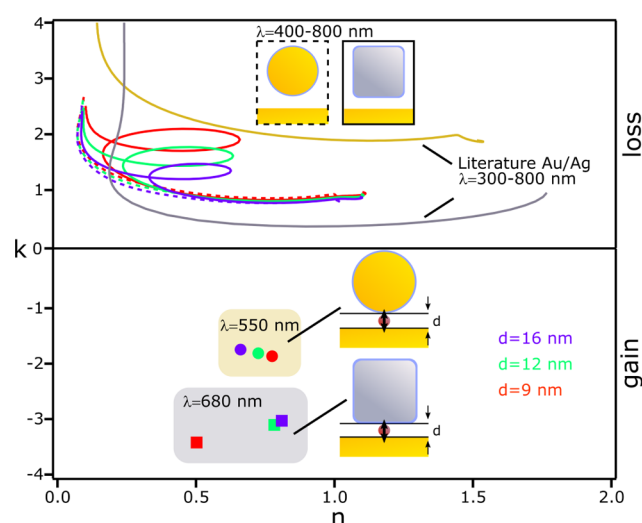


**Figure 5.** Index modulation diagram of a set of colloid-to-film-coupled nanocavities: literature values for the bulk gold and silver material are plotted between 300 and 800 nm in gold and gray, respectively. The S-parameter method is used to simulate the refractive indices from 400 to 800 nm for spherical gold (dashed line) and cubic silver (solid line) cavities at various dielectric spacings (9, 12, and 16 nm, color scheme inset). A dipole source was chosen to emulate the emitting material at 550 nm for the spherical cavity and at 680 nm for the cubic cavity.

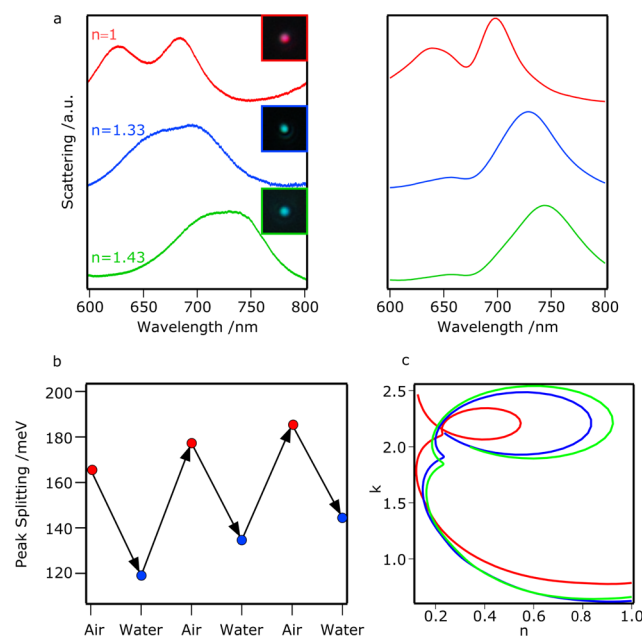


**Figure 6.** Cyclical change in the refractive index environment: (a) measured (left) and simulated (right) scattering responses of a nanocavity in different dielectric media, including air (red), water (blue), and ethylene glycol (green). (b) Reversible switching of plasmon mode hybridization by alternating the environment. (c) S-matrix calculations of the effective refractive index of the cavity structure for different ambient conditions.

follows that the loop tip can be interpreted as a resonance peak and the loop width is proportional to the FWHM of the resonance. Figure S11 describes the physical meaning of the resonances by plotting the refractive index as permittivity and permeability. An electrical mode is defined as a peak in the imaginary part of the permittivity and a magnetic mode is defined as a peak in the imaginary part of the permeability.<sup>37–39</sup>

From this it can be concluded that at spherical cavities only a magnetic mode is present and at cubic cavities electrical as well as magnetic properties occur. Depending on the excitation wavelength or cavity spacing, the real index can be changed by a factor of 2–3 and the imaginary index by 50–56% with respect to the values for bulk gold. With this scalable colloidal approach, the refractive index can be modulated in the range of metallodielectric materials.<sup>10</sup> Beyond this range, the imaginary index can become negative, whereas the real index remains unchanged by introducing an emitter within the colloidal cavity. We simulated the presence of a quantum emitter by introducing a single-wavelength dipole source whose electric field vector is perpendicular to the metallic surfaces. With this approach, we were able to determine the complex index for the sphere-to-gold film cavity at 550 nm and for the cube-to-gold film cavity at 680 nm. Consequently, with these colloid-to-film-coupled nanocavities, one can create an alternating imaginary index profile with periodic loss and gain regions.

Beyond optical computing, plasmonic systems are also highly sensitive to changes in their environments. Therefore, their optical response can be further altered by changing the parameters like the ambient RI. To study how the light–matter interactions respond when the cavity resonance is changed, we varied the dielectric environment of the system from air ( $n = 1$ ) to water ( $n = 1.33$ ) and to ethylene glycol ( $n = 1.43$ ). Figure 6 shows the scattering signals for these different ambient conditions, both in experiments and simulations. Whereas pronounced splitting is observed in air, reduced splitting is observed if the surrounding medium is changed to water or ethylene glycol. If a sample is immersed in water and dried afterward, the original peak splitting is recovered. As it is plotted in Figure 6b, this RI modulation can be cycled. We also calculated the effective refractive index using the FDTD S-parameter method. With this method, we also observed that the ambient refractive index changes the effective index to the same extent. Thus, using various colloidal cavities (Figure 5) and refractive index environments (Figure 6), we can change the real and imaginary parts of the cavity response independently.

## CONCLUSIONS

We have demonstrated the ability to tailor refractive index on a sub-wavelength scale for a set of nanocavities using spectroscopic and electromagnetic simulation methods. To ensure cost-effective fabrication on a large scale, we employed a self-assembled monolayer of thiolates and polyelectrolytes to tailor the cavity properties. This method allows us to statistically quantify the spectroscopic properties of the colloid-to-film-coupled cavities with and without embedded emitters and could be extended to create different emitter densities by using varying thiolates in the future. The resonance position and shape could be adjusted over a wide visible spectral range by introducing different colloidal materials, shapes and cavity spacings. The plasmon–exciton interaction, as a measure of the coupling strength, was confirmed by scattering spectroscopy, fluorescence lifetime measurements, and reversible refractive index sensing. The coupling strength also correlated with the effective refractive index shown by the FDTD S-parameter method. Thus, by changing the colloidal cavity parameters, the real and imaginary parts of the refractive index could be selectively and independently changed. The accurate determination of optical constants is an important step in the design of photonic nanostructures. The low-cost and scalable fabrication of tailor-

made nanocavities can therefore lead to new generation of optical circuits and light modulators.

## ASSOCIATED CONTENT

### Supporting Information

The Supporting Information is available free of charge on the ACS Publications website at DOI: 10.1021/acs.jpcc.8b12566.

UV–vis spectrum and density calculation for the AgInS monolayer; AFM, SEM, transmission electron microscopy (TEM), and additional dark-field and FLIM measurements of the studied samples; PL spectra of AgInS QDs both as a monolayer and in solution; exemplary scattering spectrum for determining coupling strength and losses in a cavity; additional FDTD simulations (PDF)

## AUTHOR INFORMATION

### Corresponding Author

\*E-mail: koenig@ipfdd.de.

### ORCID

Tobias A. F. König: 0000-0002-8852-8752

### Notes

The authors declare no competing financial interest.

## ACKNOWLEDGMENTS

This project was financially supported by the Volkswagen Foundation through a Freigeist Fellowship to TAFK. The authors acknowledge the Deutsche Forschungsgemeinschaft (DFG) within the Cluster of Excellence “Center for Advancing Electronics Dresden” (cfaed) for financial support. Thanks to Michael Göbel for the SEM and TEM measurements and to Vladimir Lesnyak from TU Dresden for the input concerning ternary metal-chalcogenides. We also want to thank Dr Ken Harris from the National Research Council Canada for his remarks and input.

## REFERENCES

- (1) Ciraci, C.; Hill, R. T.; Mock, J. J.; Urzhumov, Y.; Fernández-Domínguez, A. I.; Maier, S. A.; Pendry, J. B.; Chilkoti, A.; Smith, D. R. Probing the Ultimate Limits of Plasmonic Enhancement. *Science* **2012**, *337*, 1072–1074.
- (2) Giannini, V.; Fernández-Domínguez, A. I.; Heck, S. C.; Maier, S. A. Plasmonic Nanoantennas: Fundamentals and Their Use in Controlling the Radiative Properties of Nanoemitters. *Chem. Rev.* **2011**, *111*, 3888–3912.
- (3) Park, J.-E.; Jung, Y.; Kim, M.; Nam, J.-M. Quantitative Nanoplasmonics. *ACS Cent. Sci.* **2018**, *4*, 1303–1314.
- (4) Chikkaraddy, R.; de Nijs, B.; Benz, F.; Barrow, S. J.; Scherman, O. A.; Rosta, E.; Demetriadou, A.; Fox, P.; Hess, O.; Baumberg, J. J. Single-Molecule Strong Coupling at Room Temperature in Plasmonic Nanocavities. *Nature* **2016**, *535*, 127–130.
- (5) Chen, X.; Chen, Y.-H.; Qin, J.; Zhao, D.; Ding, B.; Blaikie, R. J.; Qiu, M. Mode Modification of Plasmonic Gap Resonances Induced by Strong Coupling with Molecular Excitons. *Nano Lett.* **2017**, *17*, 3246–3251.
- (6) Akselrod, G. M.; Argyropoulos, C.; Hoang, T. B.; Ciraci, C.; Fang, C.; Huang, J.; Smith, D. R.; Mikkelsen, M. H. Probing the Mechanisms of Large Purcell Enhancement in Plasmonic Nanoantennas. *Nat. Photonics* **2014**, *8*, 835–840.
- (7) Han, X.; Wang, K.; Xing, X.; Wang, M.; Lu, P. Rabi Splitting in a Plasmonic Nanocavity Coupled to a WS<sub>2</sub> Monolayer at Room Temperature. *ACS Photonics* **2018**, *5*, 3970–3976.

- (8) Sugimoto, H.; Yashima, S.; Fujii, M. Hybridized Plasmonic Gap Mode of Gold Nanorod on Mirror Nanoantenna for Spectrally Tailored Fluorescence Enhancement. *ACS Photonics* **2018**, *5*, 3421–3427.
- (9) Silva, A.; Monticone, F.; Castaldi, G.; Galdi, V.; Alù, A.; Engheta, N. Performing Mathematical Operations with Metamaterials. *Science* **2014**, *343*, 160–163.
- (10) Lee, J.-H.; Koh, C. Y.; Singer, J. P.; Jeon, S.-J.; Maldovan, M.; Stein, O.; Thomas, E. L. 25th Anniversary Article: Ordered Polymer Structures for the Engineering of Photons and Phonons. *Adv. Mater.* **2014**, *26*, 532–569.
- (11) Jiang, P.; Ostojic, G. N.; Narat, R.; Mittleman, D. M.; Colvin, V. L. The Fabrication and Bandgap Engineering of Photonic Multilayers. *Adv. Mater.* **2001**, *13*, 389–393.
- (12) Chen, H.; Chan, C. T.; Sheng, P. Transformation Optics and Metamaterials. *Nat. Mater.* **2010**, *9*, 387–396.
- (13) Ergin, T.; Stenger, N.; Brenner, P.; Pendry, J. B.; Wegener, M. Three-Dimensional Invisibility Cloak at Optical Wavelengths. *Science* **2010**, *328*, 337–339.
- (14) Schuller, J. A.; Barnard, E. S.; Cai, W.; Jun, Y. C.; White, J. S.; Brongersma, M. L. Plasmonics for Extreme Light Concentration and Manipulation. *Nat. Mater.* **2010**, *9*, 193–204.
- (15) Liu, N.; Mesch, M.; Weiss, T.; Hentschel, M.; Giessen, H. Infrared Perfect Absorber and Its Application As Plasmonic Sensor. *Nano Lett.* **2010**, *10*, 2342–2348.
- (16) Hugall, J. T.; Singh, A.; van Hulst, N. F. Plasmonic Cavity Coupling. *ACS Photonics* **2018**, *5*, 43–53.
- (17) Feng, L.; Xu, Y.-L.; Fegadolli, W. S.; Lu, M.-H.; Oliveira, J. E. B.; Almeida, V. R.; Chen, Y.-F.; Scherer, A. Experimental Demonstration of a Unidirectional Reflectionless Parity-Time Metamaterial at Optical Frequencies. *Nat. Mater.* **2012**, *12*, 108–113.
- (18) Feng, L.; Wong, Z. J.; Ma, R.-M.; Wang, Y.; Zhang, X. Single-Mode Laser by Parity-Time Symmetry Breaking. *Science* **2014**, *346*, 972–975.
- (19) Steiner, A. M.; Mayer, M.; Seuss, M.; Nikolov, S.; Harris, K. D.; Alexeev, A.; Kuttner, C.; König, T. A. F.; Fery, A. Macroscopic Strain-Induced Transition from Quasi-infinite Gold Nanoparticle Chains to Defined Plasmonic Oligomers. *ACS Nano* **2017**, *11*, 8871–8880.
- (20) Mayer, M.; Steiner, A. M.; Röder, F.; Formanek, P.; König, T. A. F.; Fery, A. Aqueous Gold Overgrowth of Silver Nanoparticles: Merging the Plasmonic Properties of Silver with the Functionality of Gold. *Angew. Chem., Int. Ed.* **2017**, *56*, 15866–15870.
- (21) Raevskaya, A.; Lesnyak, V.; Haubold, D.; Dzhagan, V.; Stroyuk, O.; Gaponik, N.; Zahn, D. R. T.; Eychmüller, A. A Fine Size Selection of Brightly Luminescent Water-Soluble Ag–In–S and Ag–In–S/ZnS Quantum Dots. *J. Chem. Phys. C* **2017**, *121*, 9032–9042.
- (22) Stroyuk, O.; Raevskaya, A.; Spranger, F.; Selyshchev, O.; Dzhagan, V.; Schulze, S.; Zahn, D. R. T.; Eychmüller, A. Origin and Dynamics of Highly Efficient Broadband Photoluminescence of Aqueous Glutathione-Capped Size-Selected Ag–In–S Quantum Dots. *J. Phys. Chem. C* **2018**, *122*, 13648–13658.
- (23) FDTD Solutions; Lumerical Inc. <https://www.lumerical.com/products/fdtd-solutions/> (accessed Feb 10, 2019).
- (24) Johnson, P. B.; Christy, R. W. Optical Constants of the Noble Metals. *Phys. Rev. B* **1972**, *6*, 4370–4379.
- (25) Hagemann, H. J.; Gudat, W.; Kunz, C. Optical Constants from the Far Infrared to the X-Ray Region: Mg, Al, Cu, Ag, Au, Bi, C, and Al<sub>2</sub>O<sub>3</sub>. *J. Opt. Soc. Am.* **1975**, *65*, 742–744.
- (26) Smith, D. R.; Vier, D. C.; Koschny, T.; Soukoulis, C. M. Electromagnetic Parameter Retrieval from Inhomogeneous Metamaterials. *Phys. Rev. E* **2005**, *71*, No. 036617.
- (27) Bain, C. D.; Evall, J.; Whitesides, G. M. Formation of Monolayers by the Coadsorption of Thiols on Gold: Variation in the Head Group, Tail Group, and Solvent. *J. Am. Chem. Soc.* **1989**, *111*, 7155–7164.
- (28) Love, J. C.; Estroff, L. A.; Kriebel, J. K.; Nuzzo, R. G.; Whitesides, G. M. Self-Assembled Monolayers of Thiolates on Metals as a Form of Nanotechnology. *Chem. Rev.* **2005**, *105*, 1103–1170.
- (29) Reynaud, C. A.; Duché, D.; Le Rouzo, J.; Nasser, A.; Nony, L.; Pourcin, F.; Margeat, O.; Ackermann, J.; Berginc, G.; Nijhuis, C. A.; et al. Enhancing Reproducibility and Nonlocal Effects in Film-Coupled Nanoantennas. *Adv. Opt. Mater.* **2018**, *6*, No. 1801177.
- (30) Decher, G. Fuzzy Nanoassemblies: Toward Layered Polymeric Multicomposites. *Science* **1997**, *277*, 1232–1237.
- (31) Izquierdo, A.; Ono, S. S.; Voegel, J. C.; Schaaf, P.; Decher, G. Dipping versus Spraying: Exploring the Deposition Conditions for Speeding Up Layer-by-Layer Assembly. *Langmuir* **2005**, *21*, 7558–7567.
- (32) Zengin, G.; Wersäll, M.; Nilsson, S.; Antosiewicz, T. J.; Käll, M.; Shegai, T. Realizing Strong Light-Matter Interactions Between Single-Nanoparticle Plasmons and Molecular Excitons at Ambient Conditions. *Phys. Rev. Lett.* **2015**, *114*, No. 157401.
- (33) Törmä, P.; Barnes, W. L. Strong Coupling Between Surface Plasmon Polaritons and Emitters: A Review. *Rep. Prog. Phys.* **2015**, *78*, No. 013901.
- (34) Hoang, T. B.; Akselrod, G. M.; Argyropoulos, C.; Huang, J.; Smith, D. R.; Mikkelsen, M. H. Ultrafast Spontaneous Emission Source Using Plasmonic Nanoantennas. *Nat. Commun.* **2015**, *6*, No. 7788.
- (35) Schnepf Max, J.; Brasse, Y.; Gößler Fabian, R.; Steiner Anja, M.; Obermeier, J.; Lippitz, M.; Fery, A.; König Tobias, A. F. Single Particle Spectroscopy of Radiative Processes in Colloid-to-Film-Coupled Nanoantennas. *Z. Phys. Chem.* **2018**, *232*, 1593–1606.
- (36) Mayer, M.; Tebbe, M.; Kuttner, C.; Schnepf, M. J.; König, T. A. F.; Fery, A. Template-Assisted Colloidal Self-Assembly of Macroscopic Magnetic Metasurfaces. *Faraday Discuss.* **2016**, *191*, 159–176.
- (37) Brasse, Y.; Müller, M. B.; Karg, M.; Kuttner, C.; König, T. A. F.; Fery, A. Magnetic and Electric Resonances in Particle-to-Film-Coupled Functional Nanostructures. *ACS Appl. Mater. Interfaces* **2018**, *10*, 3133–3141.
- (38) Dolling, G.; Enkrich, C.; Wegener, M.; Zhou, J. F.; Soukoulis, C. M.; Linden, S. Cut-Wire Pairs and Plate Pairs as Magnetic Atoms for Optical Metamaterials. *Opt. Lett.* **2005**, *30*, 3198–3200.
- (39) Mayer, M.; Schnepf, M. J.; König, T. A. F.; Fery, A. Colloidal Self-Assembly Concepts for Plasmonic Metasurfaces. *Adv. Opt. Mater.* **2019**, *7*, No. 1800564.